Computational Design of a Supersonic Expansion-Compression Experiment for Turbulence Model Development

Nathan E. Miller *, Anshuman Pandey †, Matthew Barone ‡, Kyle P. Lynch §, Steven J. Beresh ¶
Sandia National Laboratories, Albuquerque, NM, 87185

To assist in the planning of ongoing wind tunnel tests of a tandem expansion-compression geometry at Sandia National Laboratories, simulations of the experimental conditions were conducted using multiple turbulence models. Simulation results demonstrate the expected flow topology, but more importantly, predict the expected values of key variables of interest in the flow. The results show the spanwise variation in the separation and reattachment locations in the compression corner. This spanwise variation is related to the existence of streamwise-oriented structures which persist well downstream of reattachment and leave a visible footprint in the wall shear stress and wall heat flux. Until detailed reporting of the experimental data is available, limited preliminary data are included here for comparison to the simulation results. The present computational results are being used in the experimental planning, in particular to optimally locate instrumentation within the complex three-dimensional flow.

Nomenclature

Ma	Mach number
q_w	Wall heat flux
r	Recovery factor
R	Gas constant
Re_τ	Friction Velocity Reynolds number (= $u_\tau \delta / \nu_w$)
Re_θ	Momentum thickness Reynolds number (= $U_e \theta / \nu_e$)
T	Temperature
u'	Turbulent fluctuations of the streamwise velocity
u_τ	Friction velocity (= $\sqrt{\tau_w / \rho_w}$)
U	Reynolds-averaged streamwise velocity
γ	Specific heat ratio
δ	Boundary layer thickness
θ	Momentum thickness
μ	Dynamic viscosity
ν	Kinematic viscosity (= μ / ρ)
ω	Vorticity
ρ	Density
τ_w	Wall shear stress

Sub/superscript

aw	Adiabatic wall
e	Boundary layer edge value
w	Wall value
∞	Freestream values, outside the boundary layer
$+$	Inner scaled values

*Senior Member of the Technical Staff, Aerosciences, AIAA Sr. Member, nmille1@sandia.gov
†Senior Member of the Technical Staff, Aerosciences, AIAA Member, apandey@sandia.gov
‡Principal Member of the Technical Staff, Aerosciences, AIAA Associate Fellow, mbarone@sandia.gov
§Principal Member of the Technical Staff, Diagnostics for External Environments & Hypersonics, AIAA Sr. Member, klynch@sandia.gov
¶Distinguished Member of the Technical Staff, Aerosciences, AIAA Fellow, sjberes@sandia.gov

I. Introduction

The expansion-compression configuration introduces a number of challenges for Reynolds-averaged Navier–Stokes (RANS) models. The sudden mean expansion and subsequent favorable pressure gradient forms a non-equilibrium boundary layer, and relaminarization can occur [1, 2]. Streamline curvature is also typically present in this region. As the boundary layer encounters the compression corner, the re-compression shock and adverse pressure gradient can cause separation, and subsequent reattachment, of the boundary layer. The behavior of the shock/boundary-layer interaction differs from canonical flows due to the state of the expanded, non-equilibrium boundary layer. The streamline curvature can also cause a Görtler-like instability, with generation of associated streamwise-oriented vortical structures near the wall.

The combination of an expansion and compression corner has been studied both computationally and experimentally, using a variety of geometries. In the 1980s, Zheltovodov et al. conducted a series of experiments studying a tandem expansion-compression geometry similar to that studied here (e.g., [3]). That work was at Mach 2.9 and with a shorter ramp than used herein. Later, both Fang et al. [4] and Xie et al. [5] conducted direct numerical simulations (DNS) of those experiments and studied the impact of Reynolds number on the unsteady and three-dimensional (3D) signatures of the flow. Others, like Kianvashrad and Knight [6] have conducted large-eddy simulation of the same.

Another expansion-compression geometry that has been studied in recent years is the cone-slice-ramp geometry, which has been primarily studied in hypersonic flows. Vogel et al. [7, 8] and McKiernan and Schneider [9] focused on one exemplar studied in the Boeing/AFOSR Mach-6 Quiet Tunnel while Sadagopan et al. [10] and Pandey et al. [11, 12] studied a somewhat different geometry at Mach numbers 5 and 8 in the Sandia National Laboratories (SNL) Hypersonic Wind Tunnel.

Also recently, Tichenor et al. [13] studied the impacts of pressure gradients on supersonic boundary layers by using a smooth expansion-compression geometry in a Mach 4.9 tunnel. Nicholson et al. [14] simulated those experiments using DNS in order to study the limitations of RANS models when simulating such gradients. Early efforts to validate RANS models against expansion-compression data sets were documented in Knight et al. [15].

With an expectation of producing a high-quality experimental dataset that will be used for turbulence model development and simulation validation, SNL is planning a series of wind tunnel tests in the SNL Trisonic Wind Tunnel (TWT) wherein a tandem expansion-compression geometry will be studied in supersonic flow at nominal Mach numbers of 1.5, 2.0, and 2.5 (Sect. II). While the ultimate goal of this experimental effort is to generate data for training and validation of improved RANS models, RANS analysis with current turbulence models can also play a useful role in designing the experiment. The anticipated measurements will be taken in a wind tunnel with non-trivial upstream contraction geometry and a finite-width test section, thus adding corner-flow complexity to the flow. The rectangular test section of the TWT creates the corner flow effects which are expected to modify the SBLI length scales. RANS can be useful for assessing non-uniformity of the flow in the test section, as shown in Childs et al. [16], for example. It can also aid in identifying areas of interest, to guide instrumentation placement within the flow, such as regions of boundary layer separation, possible relaminarization, streamwise streaks in wall heat flux (q_w), etc. To that end, two turbulence models were applied to two of the Mach numbers to be studied in this problem (Sect. II). They show distinctly different results for key quantities of interest in the dynamic regions of the flow (Sect. III).

II. Methods

The forthcoming experiments will be conducted in SNL's TWT. The TWT is capable of producing centerline Mach numbers across the subsonic to supersonic range by varying the nozzle and outlet geometries. For these experiments, supersonic nozzles that produce test-section Mach numbers of 1.5, 2.0, and 2.5 will be used. Only the Mach 2.0 and 2.5 cases were simulated as part of this work. While the test section of TWT is typically square with dimensions of 305×305 mm, for these experiments the tunnel's "half-nozzle" hardware will be installed in the tunnel. This configuration cuts the tunnel in half by extending the inlet contour to the nozzle centerline in the nozzle throat before fairing into a flat surface which extends into the test section. This same hardware has been used for a variety of previous experiments in TWT (e.g., [17, 18]). The half-nozzle floor will end in the test section and will be followed immediately by a ramp with a height of 12.7 cm oriented 25° from the tunnel floor, thus creating the expansion and compression corners (Fig. 1, Upper). The half-nozzle floor results in the tunnel dimensions being 305 mm wide by 146 mm tall (for Mach 2.5) or 149 mm tall (for Mach 2.0) at the expansion corner of the ramp ($x = 0$); the tunnel nozzle is still expanding at this point. The ramp, combined with the continued expansion of the tunnel nozzle leads to a cross section of 305×279 mm at the downstream end of the ramp and for the rest of the test section.

Modeling of the experiment was conducted using SNL's Parallel Aero Reentry Code (SPARC). SPARC is SNL's

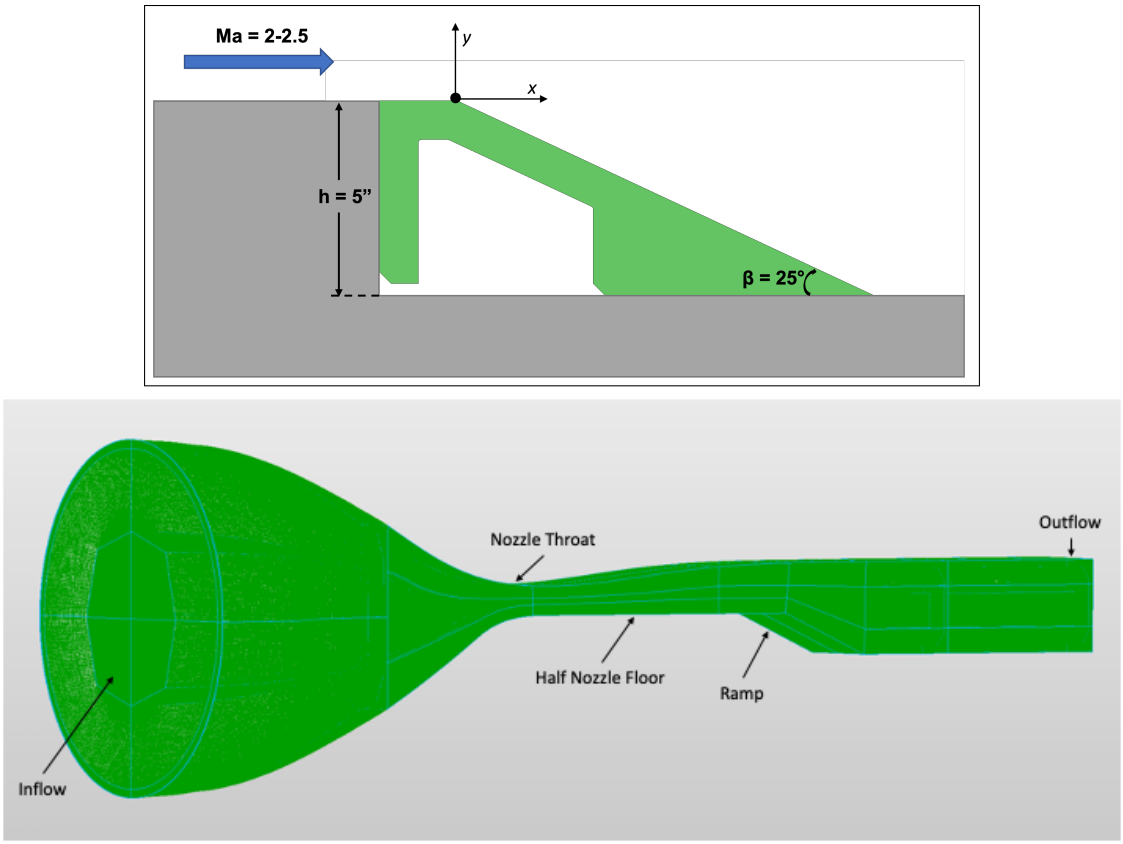

Fig. 1 Images of (Upper) a schematic of the ramp hardware as placed in the TWT as well as (Lower) the CFD mesh for the Mach 2.0 simulations showing the whole tunnel.

exa-scale-ready finite-volume computational fluid dynamics (CFD) code and has been used for a variety of problems [19–21] including previous simulations of the TWT for the axisymmetric transonic bump experiment and validation challenge hosted by SNL [22, 23]. SPARC is capable of a variety of different modeling fidelities from Newtonian aerodynamics to DNS and includes multiple RANS closure models. Because the focus of this work is on investigating the 3D phenomena induced by the expansion-compression geometry two different RANS closure models were used so that differences could be studied. The baseline, linear Spalart–Allmaras (SA) model and the version of the SA model extended to include the nonlinear Quadratic Constitutive Relation (SA-QCR) were both used. Previous works have shown that the inclusion of the QCR term into RANS models improves predictions of 3D effects in complex flows (e.g., [24–26]). The actual model implemented in SPARC is the SA-QCR2000 model*. A total of four simulations were performed using SA and SA-QCR for each of the centerline Mach numbers 2.0 and 2.5.

The full TWT from plenum to outflow, including the nozzle and the hardware to split the tunnel and produce the expansion-compression flow, was meshed for each Mach number (Fig. 1, Lower). The fully-structured, multi-block meshes (one for each Mach number) consist of over 42M cells. The simulations were run with air as the working gas using the perfect gas model and Sutherland's viscosity law. The inflow boundary condition was specified with a total pressure of 113.76 kPa, a total temperature of 345.0 K, and a negligible velocity. It is expected that other inflow conditions which produce other Reynolds numbers will also be studied in the experiments. Because the broad majority of the flow at the outflow plane would be supersonic, a supersonic-outflow boundary condition was used. Additionally, the outflow plane in the mesh is defined farther downstream than the physical downstream end of the usable test section of the TWT. This was done to stop observed transients near the outflow plane from delaying or preventing convergence, and to reduce the possibility that subsonic flow near the walls would propagate erroneous pressure effects into the region where comparisons would be made to TWT flows.

*Details of SA-QCR2000 model can be found at https://turbmodels.larc.nasa.gov/spalart.html#qcr2000 and in Spalart [27]

Table 1 Boundary layer and flow conditions from the simulations taken at $x \approx -5\delta$ (upstream of the leading corner of the ramp). Wall-based quantities are reported with respect to the half-nozzle floor, not the opposite tunnel wall. Both the compressible and *incompressible* equivalents for Re_θ are shown [28].

Ma_∞	RANS	U_∞ [m/s]	ρ_∞ [kg/m^3]	δ_{99} [m]	Re_θ	τ_w [Pa]	Re_τ	T_w/T_{aw}
2.0	SA	549.4	0.275	0.0118	10095(*6647*)	84.4	2171	1.02
	SA-QCR	549.8	0.274	0.0123	10255(*6725*)	81.6	2226	1.02
2.5	SA	613.8	0.162	0.0124	7446(*4081*)	56.2	1278	1.03
	SA-QCR	614.0	0.161	0.0130	7691(*4188*)	55.1	1326	1.03

Table 2 Boundary layer conditions taken at $x \approx -5\delta$ from the preliminary PIV in TWT.

Ma_∞	U_e [m/s]	ρ_e [kg/m^3]	$\delta_{99.5}$ [m]	Re_θ	τ_w [Pa]	Re_τ
2.0	542.2	0.510	0.0106	17656	125.2	3200

All walls were set to an isothermal condition of 332.9 K. This was chosen based on previous experience with TWT heating up over the course of repeated runs performed in a single day. Equivalent adiabatic wall temperatures ($T_{aw} = T_e + 0.5rU_e^2(\gamma - 1)/(\gamma R)$) were calculated for each simulation at a location just upstream of the expansion corner (see Sect. III.A) and were found to be between 323 and 328 K. Thus, the simulations functioned as though they had very nearly adiabatic walls, at least in the region upstream of the ramp.

A turbulent trip location was specified in the converging portion of the nozzle. Upstream of this location the turbulence model remained off. It is suspected that in the experiments the boundary layer will be turbulent upstream of the nozzle, will be thinned and possibly relaminarize in the nozzle throat, and then grow on all of the tunnel walls into the test section. Confirmation of this will be sought during the experiments, but until then a specified trip location of 69 cm upstream of the narrowest point of the throat was chosen. This is half the distance between the inflow boundary and the throat (1.37 m). The various plenum pressures that will be studied in the experiments may also alter the effective upstream transition location.

A total of 1440 CPU cores were used on SNL's Manzano high-performance computing cluster for each of these simulations. Convergence of the simulations took considerable time. Many flowthrough times were necessary to get the bulk topology of the expansion, shock, and separation bubble to reach stationarity after initial transients. Using the distance from the nozzle throat to the mesh outflow plane and the centerline velocity taken directly above the expansion corner, it took > 23 flowthrough times for the separation location to no longer move in the SA simulation of the Mach 2 flow. Over 50 additional flowthrough times were then run before the results presented below were taken. At that point the spanwise (z) profiles of quantities of interest (e.g., streamwise vorticity) stopped changing appreciably.

III. Simulation data analysis

A. Upstream Behavior

During the experiments in the TWT, flow data will be collected at $\approx 5\delta$ (where δ is the boundary layer thickness) upstream of the ramp corner to ensure that the inflow conditions to the expansion are well understood. A limited set of preliminary TWT runs have already been completed at Mach 2.0 while collecting 2D Particle Image Velocimetry (PIV) data at only this upstream location. Here we report various key variables from this location from both the simulated datasets (Table 1) and the preliminary TWT runs (Table 2). This includes the δ needed to define the 5δ location upstream. Differences between the two turbulence closures are minimal, but clearly identifiable even upstream of the expected 3D complexities around the expansion, ramp, and compression geometries.

The preliminary data in Table 2 were produced from TWT runs where the stagnation condition in the plenum had a total pressure of 206.84 kPa and a total temperature of 325 K. This pressure is much higher than was used in the

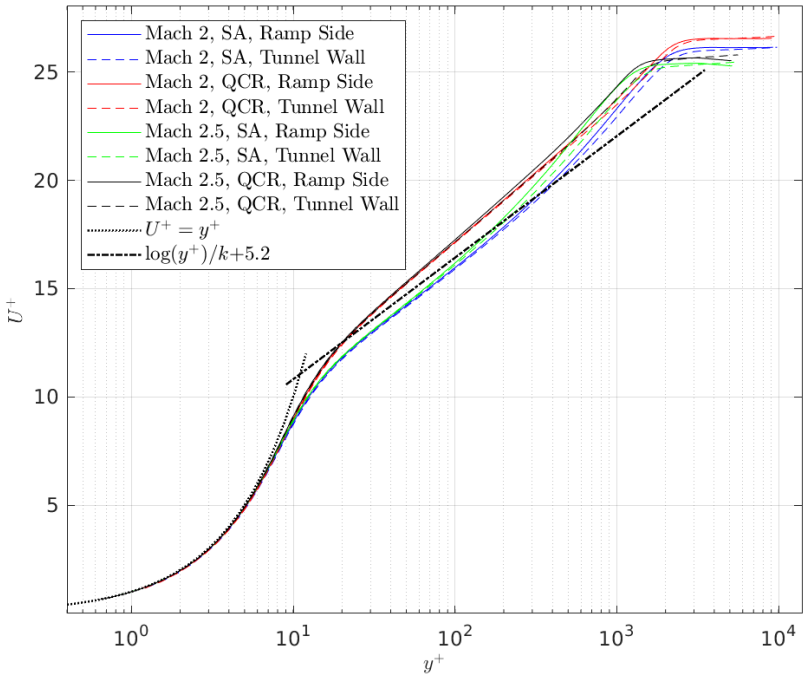

Fig. 2 Inner-scaled profiles of U from both the tunnel wall and on the half-nozzle floor upstream of the ramp at $x \approx -5\delta$. Compressibility has been accounted for by the Van Driest approach [29].

simulations. Additionally, the TWT was venting to atmosphere while the simulations allowed the pressure to develop based on the supersonic inviscid expansion which resulted in a mean static pressure of ≈ 8 kPa at the simulated outflow plane for the Mach 2.0 simulations (≈ 4 kPa for Mach 2.5). It is not known as of now what the effective mean static pressure is in the TWT at the outflow of the test section. So while the differences in the total pressures and the static back pressures may have been relatively similar between the simulations and the TWT runs, the ratios of the two were likely quite different. As a result we would expect that inviscid features (e.g., U_∞, shock locations, etc.) of the flow should be quite similar (as they are geometry-dominated, as long as the Reynolds number is high enough) but that the viscous features (e.g., wall shear stress (τ_w), Re_τ, etc.) could differ considerably. As can be seen, the Reynolds numbers for the TWT runs were considerably higher than in the RANS, but the boundary layer thickness and edge velocity were quite similar. Future TWT runs will vary the stagnation conditions to study multiple Reynolds numbers, and commensurate simulations may be performed so more direct comparisons can be made.

Profiles of the x-oriented velocity component (U) upstream of the ramp show fully developed turbulent boundary layers on multiple tunnel walls (Fig. 2). The profiles are taken from the half-nozzle floor (i.e., the ramp side of the tunnel) and from the upper tunnel wall (i.e., the ceiling) on the center plane (z = 0) of the tunnel both at $x \approx -5\delta$, upstream of the ramp corner. The SA and SA-QCR models return slightly different profile shapes for the log layer. While the QCR model predicted an almost perfect match to the log-law before the Van Driest transformation was applied (not shown) its predictions are slightly higher than the canonical log layer behavior after compressibility was accounted for [29]. Similarly while SA predicted lower than expected values pre-transformation, the transformed values align quite well with expectations for much of the expected log region. The SA predictions do tend to show a larger wake region than do the QCR predictions. These results are consistent across both Mach numbers and both on the tunnel wall and the half-nozzle floor. One noticeable difference between the tunnel wall and half-nozzle floor profiles is that the profiles from the ramp side tend to show a larger overshoot in the wake region than do the profiles on the tunnel ceiling. While each pair of lines is relatively indistinguishable below $y^+ \approx 150$, they then begin to diverge, with the half-nozzle floor profiles always trending higher, before then coming back together in the freestream.

B. Centerplane Behavior

Contours of U taken from the plane through the center of the tunnel test section show the topology of the flow field (Fig. 3); note the upstream boundary layer, the expansion fan, the separation and reattachment in the compression corner,

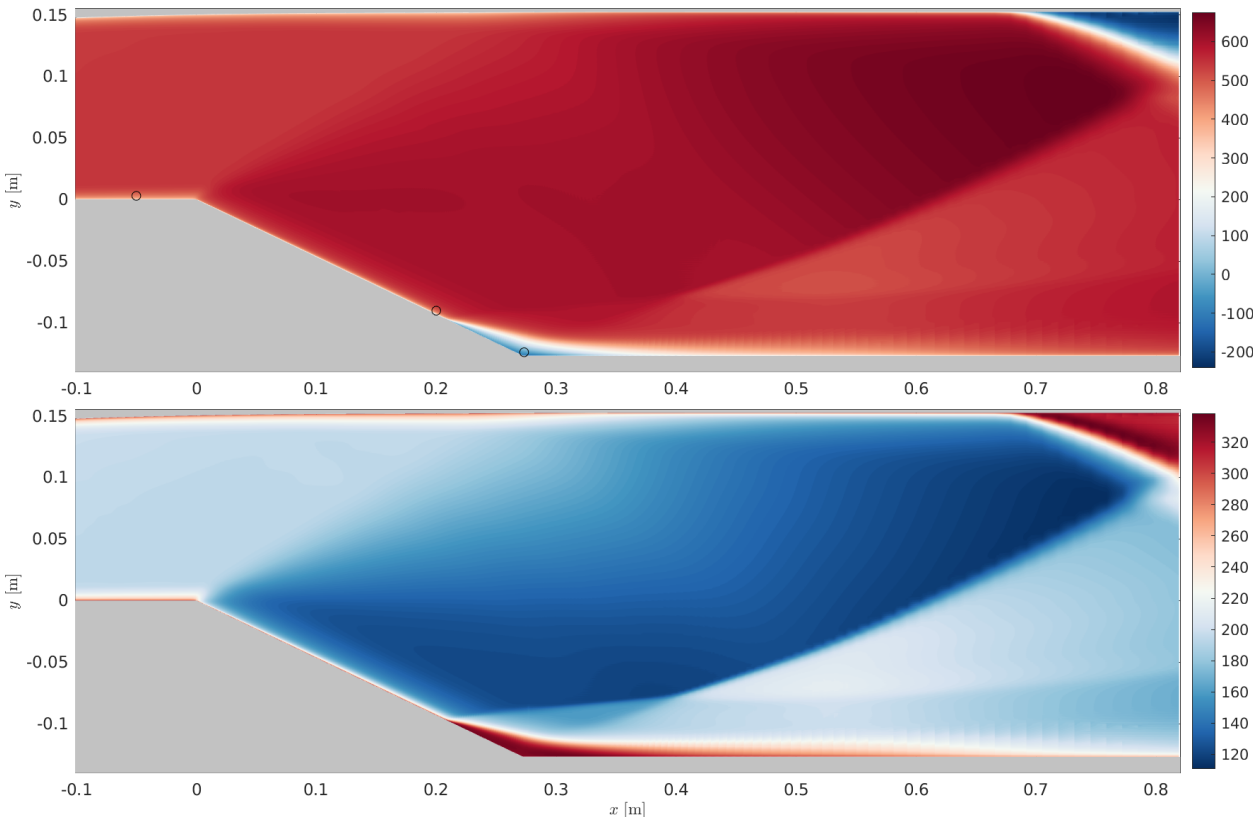

Fig. 3 Contours of (Upper) U [m/s] and (Lower) T [K] on the central plane of TWT taken from the Mach 2 SA case. The circular markers indicates the locations of the profiles shown in Figs. 5 and 6.

the λ shock, and the shock-induced separation on the upper tunnel wall farther downstream. While only the Mach 2 case is shown, the Mach 2.5 case exhibits all the same topological phenomena albeit with a slightly different velocity magnitude, a smaller separation region (discussed below), and shallower angles for the expansion fan and shock. The shallower shock angle results in the upper wall's shock-induced separation happening much further downstream, but this puts it beyond the TWT test section and into the extended portion of the mesh that was added to prevent issues related to the outflow boundary. For this reason and because of optical access issues in the TWT, it is not expected that the shock induced separation on the upper wall will be observed during the experiments.

Temperature contours on the same central plane exhibit the same topological features but demonstrate the heating expected in the boundary layers and in the separated region in the compression corner (Fig. 3, Lower). While the isothermal wall resulted in an approximately adiabatic wall condition in the upstream section, it is clear from the temperature contours that that behavior will not be present on the ramp face—where the flow is clearly much cooler than in the upstream region—or in the recirculation region where the flow is much hotter (see Sect. III.E).

C. Separation and Reattachment

As expected, the separation and reattachment lines differ significantly between the SA and SA-QCR simulations (Fig. 4). Because of the 3D effects in the flow, the separation and reattachment lines vary as a function of the spanwise (z) coordinate in the tunnel. For this work, the separation and reattachment were identified using the wall shear stress magnitude (τ_w) by looking for the local minimum values along each streamwise mesh line. Complexities related to vorticity in the corners make identification of separation difficult near the sidewalls so only the definitively identifiable portions are include here. See Sect. III.E for more details.

Generally, the QCR model predicts a smaller separation region in the compression corner, with both the separation and reattachment lines being closer to the compression corner across most of the span than was observed in the SA simulations. While this observation was generally true regardless of the spanwise location, the actual separation and

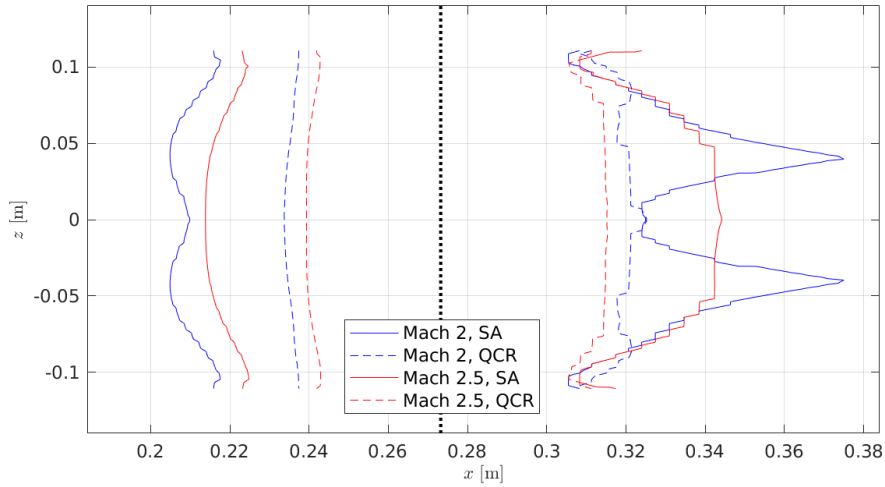

Fig. 4 The separation and reattachment lines across the span of the tunnel for each of the four simulations. The dotted line at $x = 0.272$ m indicates the location of the compression corner.

reattachment points varied considerably with z from what was observed on the center plane.

D. Spanwise Profiles

One expectation for this flow was that the streamline curvature around the flow separation in the compression corner would lead to 3D Görtler-like vortices initiated on the ramp face which would then propagate through the separation region and lead to local concentrations of heating and shear stress on the wall downstream. While the wall effects will be discussed in Sect. III.E, here we demonstrate some of the 3D effects that do appear within the near-wall flow.

First, examining spanwise profiles of U (Fig. 5), each 3 mm above the floor, at the three streamwise locations depicted in Fig. 3 reveals no obvious 3D effects over most of the span on the ramp face, except those near the sidewalls where corner flow effects were expected (e.g., [25]). Upstream of the expansion corner the corner flow vortices are relatively small and although corner-flow vorticity cannot necessarily be seen in U the “upstream" line shows only a narrow region where the sidewall boundary layer is impacting the streamwise flow. This upstream line was taken from 3 mm above the floor ($\approx \delta/4$) at the same location upstream of the expansion corner as was used in Fig. 2. As the flow traverses past the expansion corner the corner flow vorticity tends to grow considerably and begin imparting effects farther towards the tunnel centerline.

Once the flow separates in the compression corner, looking at profiles within the recirculation region, considerably more three dimensionality becomes apparent. The corner flow effects exhibit an influence further from the wall (following a topology like that studied in the compression corner in Sabnis et al. [30]), but also, within the central corridor of the flow ($|z| < 0.1$ m) oscillations in the velocity become apparent and point towards the presence of 3D vorticity that may not be attributable to the corner flow effects. This is most apparent for the Mach 2 case simulated with SA.

Additionally, there is considerable variation in the modeled velocities within the recirculation regions with the different models. Differences of > 150 m/s are seen between SA and SA-QCR at some spanwise locations for cases with the same Mach number. This could be because the strengths of the recirculations themselves are different between the models and/or because the volume of the recirculation regions are different between the models and the spanwise profiles are being taken at different locations relative to the outer boundary of the recirculation volume (i.e., closer to the $U = 0$ boundary). The latter of these likely explains the near-zero velocities exhibited by the SA-QCR simulations, as those simulations result in much smaller recirculation volumes than do the corresponding SA simulations. For the Mach 2.5 SA-QCR simulation specifically, the profile is taken so near to the volume boundary that for most of the span U is ≈ 0 and is even slightly positive (not recirculating) around $|z| = 0.1$ m where the corner effects interacts with the central corridor.

While the U profiles do not necessarily show evidence of Görtler-like vortices on the ramp upstream of the separation, they clearly show 3D effects immediately after separation. To identify streamwise oriented vorticity that would be indicative of Görtlerian effects, the x-oriented component of the vorticity vector (i.e., ω_x) was also examined on the

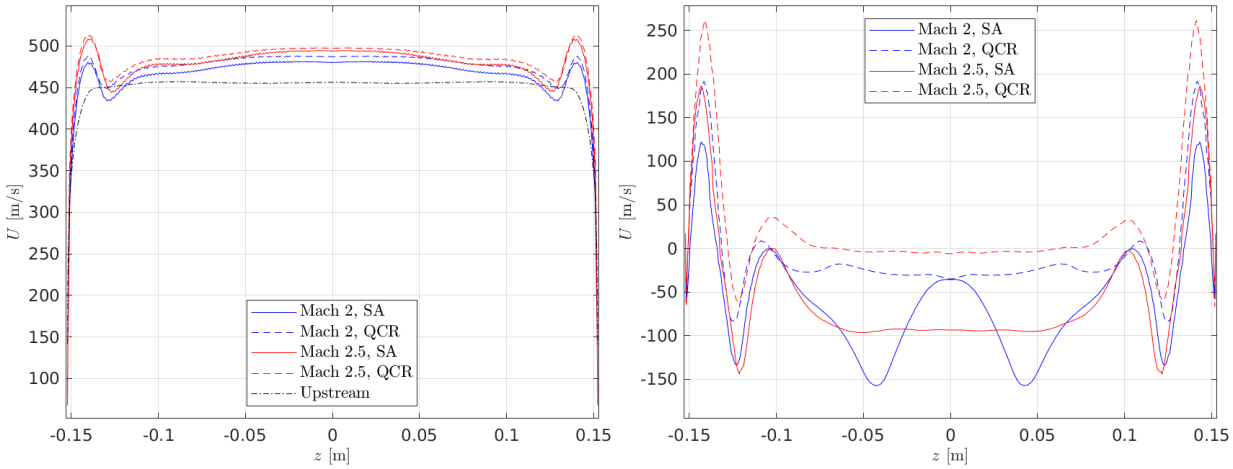

Fig. 5 Spanwise profiles of U (Left) in the boundary layer just upstream of the separation and (Right) within the recirculation region above the compression corner. The black dot-dashed line is taken from $\approx 5\delta$ upstream of the expansion corner from the Mach 2 SA case.

same spanwise profiles near the wall (Fig. 6).

At the profile location on the ramp face, upstream of the separation, the corner flow vortices are clearly visible in the oscillatory behavior of ω_x near the side walls (Fig. 6, Left). When compared to the reference line taken from upstream of the expansion corner it becomes very apparent how much the corner flow vortices have expanded away from the walls and into the flow. Upstream of the expansion, the corner flow vorticity did not extend more than approximately 3 mm from the side walls. It is not necessarily clear how much of the vorticity seen at the point where the flow is approaching the separation line on the ramp face is directly attributable to the corner vortices expanding (versus some other effect), but clearly the vorticity at least multiple centimeters in from the sidewalls is being influenced.

Multiple additional effects can be seen in ω_x once the flow separates in the compression corner (Fig. 6, Right). First, the magnitudes of the most extreme peaks in the vorticity increase by about a factor of four. Second, the vorticity very near the walls ($|z| > 0.15$ m) switches signs and increases by a factor much greater than four (cropped from the figure). In complex 3D corners where flow separation is present, it has been shown that the direction of circulation of the near-wall flow switches due to the interaction with the recirculation vortex in the separated region [30–32]. This can also be seen in the wall shear stress data below. Third, in the SA-QCR simulations, the most medial of the peaks just upstream of the separation nearly disappear and for the Mach 2 case even change signs at around $|z| = 7$ cm. Finally, for the Mach 2 SA simulation additional vorticity peaks appear within the central corridor of the flow, which exhibited zero vorticity just upstream. This may be the formation of streamwise vortices like those observed by Zhuang et al. [33], and/or could be a counter-rotating response to the corner flow vortices' continued incursion into the central corridor.

E. Wall Fluxes

The wall heat flux and wall shear stress exhibit large spanwise variations, especially in the separated region and downstream of the reattachment (Fig. 7). Only the Mach 2 SA case is depicted as it gives the most extreme visual representation of the flux behaviors. While the other simulated datasets differ, the same primary flow features can be easily identified. The separation line is clearly identifiable in $\tau_{w,x}$ for most of the tunnel span and was shown previously for each of the simulations (Fig. 4). The reattachment line is somewhat more complicated and is a combination of both the x-oriented and z-oriented components of the shear stress vector. The reattachment lines shown previously were determined by the location at which τ_w reached a local minimum. Because of the complexity of the 3D flow in the corners, separation and reattachment are less clearly identifiable. The corner flow vortices may be creating a spanwise-based separation based primarily on $\tau_{w,z}$ as depicted by Williams and Babinsky [32]. No effort has yet been made to extensively characterize the flow topology in these corners, but may be done in the future depending on the observed behavior in the tunnel experiments.

The reattachment line itself has a lobed structure, but the spanwise spacing of the lobes is significantly different than has been observed in flows where Görtler vortices have been identified (e.g., [33]). It may be that these SA results are

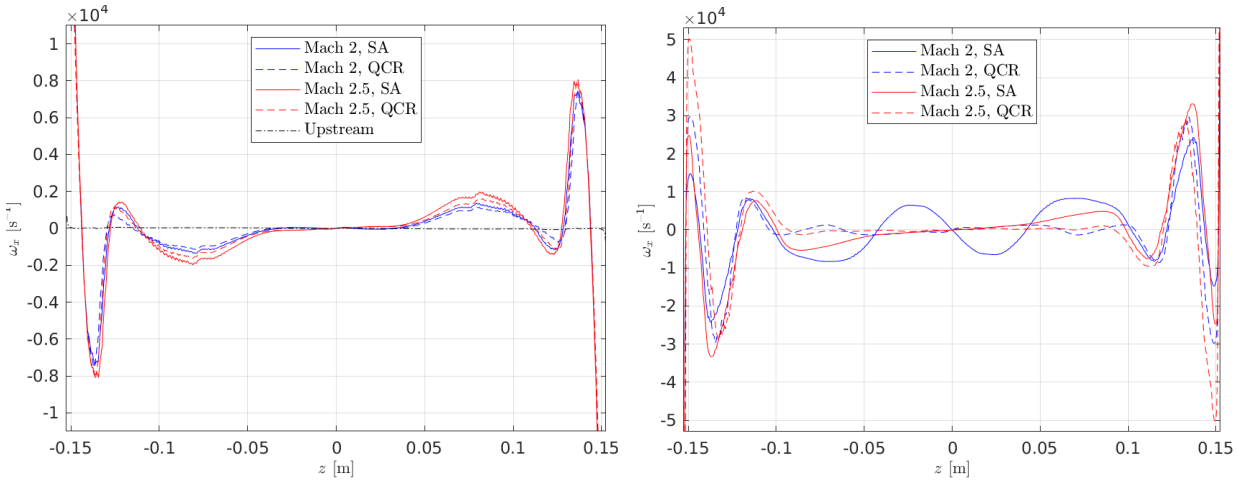

Fig. 6 Spanwise profiles of ω_x (Left) in the boundary layer upstream of the separation and (Right) within the recirculation region above the compression corner. The black dot-dashed line is taken from $\approx 5\delta$ upstream of the expansion corner from the Mach 2 SA case.

simply unphysical or that some other effect is being captured. Regardless, the lobed structures leads to the considerable spanwise variation in both the heat flux and the shear stress propagating well downstream of the reattachment line.

Upstream of separation, the wall heat flux is negative on the ramp face, meaning that the wall is warmer than and therefore heating the flow, as mentioned above related to the temperature field (Fig. 3). Downstream of the separation shock the post-shock flow is much hotter than the isothermal wall and results in the sign change in the heat flux and the considerable heating of the wall by the flow. While the most extreme local heat fluxes are seen in the complex 3D flow regions just downstream of the corner-flow-compression-corner interaction, there is still considerable heating in the central portions of the flow around the line of reattachment, and especially within the lobed structures seen just after reattachment. The fluxes in these regions will be of particular interest for the experiment as they are likely regions that the RANS models are not predicting well.

Also of note here is the behavior of the fluxes along the ramp face. Starting at each spanwise end of the expansion corner (i.e., at the left corners of each image) a variation in all the wall fluxes can be seen expanding from the sidewalls towards the tunnel centerline. This is clearly the footprint of the effects seen expanding from the sidewalls discussed above and identified in the streamwise vorticity line taken at $x = 0.2$ m (Fig. 6, Left). Although the corner flow effects are very small upstream of the expansion corner, the presence of the expansion causes this significant propagation of vorticity into the flow.

Examination of streamwise traces of the wall fluxes down the middle of the tunnel ($z = 0$) helps to elucidate the difference between the models and the Mach numbers (Fig. 8). The separation and reattachment locations at the tunnel centerline are identified by using the sign of $\tau_{w,x}$, and again the differences in the sizes of the recirculation regions are apparent. Interestingly, for the Mach 2 case, even though the two models predict the same reattachment point, their respective behavior after reattachment varies considerably, with different slopes resulting in τ_w values that differ by 47% at $x = 0.55$ m. In contrast, for the Mach 2.5 case, while the reattachment points differ considerably, the two models show somewhat similar behaviors after reattachment and appear to be converging to a similar τ_w value at the end of the domain.

For the centerline behavior of q_w, the differences in the separation locations between the two models are again apparent, even if very similar fluxes are predicted right in the compression corner. Immediately after the compression corner the two models behave quite differently, with the SA model always predicting higher heat fluxes than the SA-QCR model, for both Mach numbers. Note that the heat fluxes hit their respective local maxima at the point of reattachment as identified from $\tau_{w,x}$. The observed differences in the predicted wall heat fluxes from different RANS models were a primary motivator for this planned experimental work and subsequent turbulence model development.

Spanwise profiles of the wall fluxes for each of the simulation show the spanwise variability differences between the two models. Figure 9 shows profiles of τ_w taken just upstream of separation and just downstream of reattachment while Fig. 10 shows the same for q_w. It is clear from these that the SA model predicts a much higher level of spanwise variation than does SA-QCR and predicts more streamwise coherency of clearer definition.

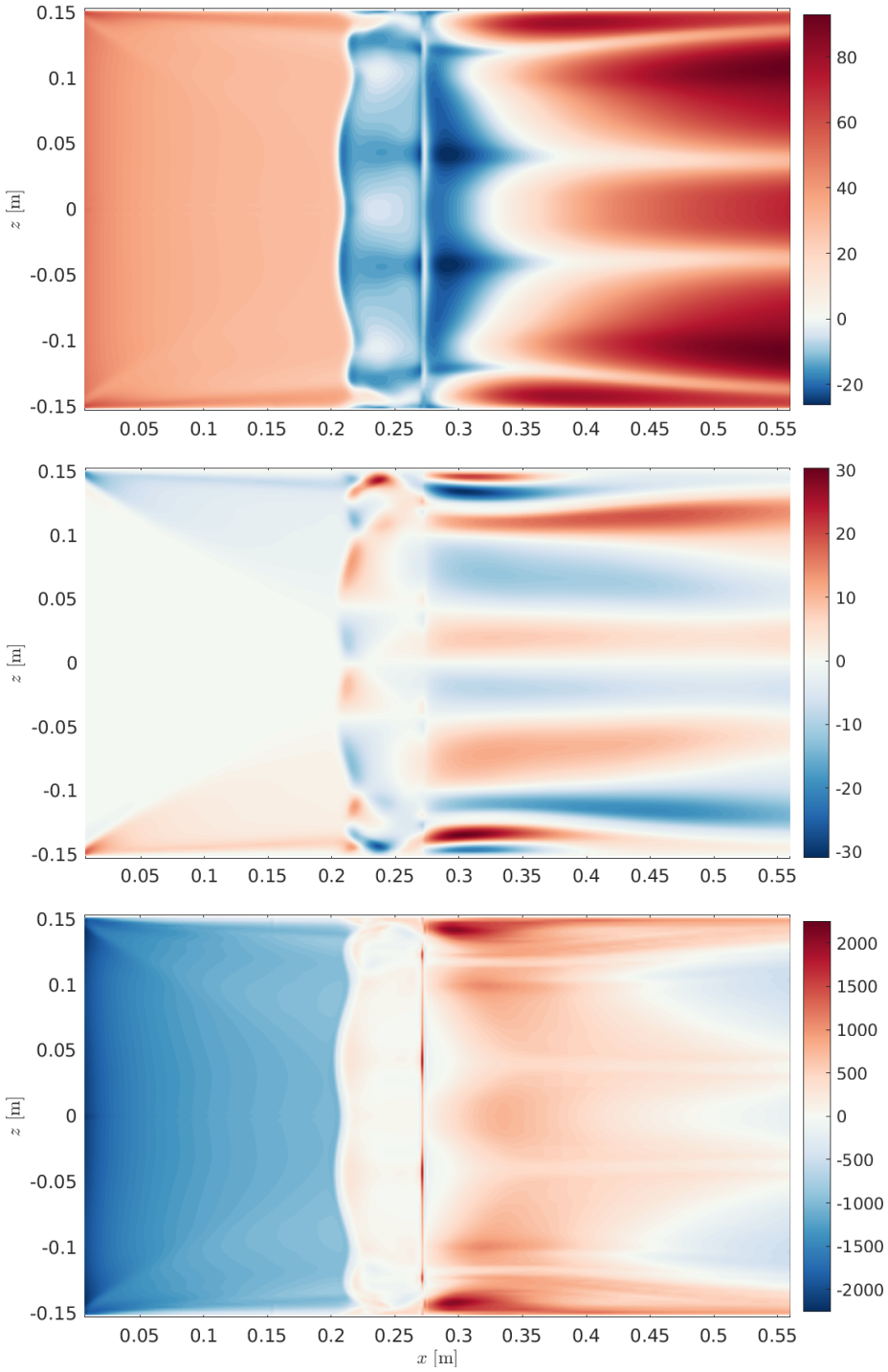

Fig. 7 Contours of (Upper) $\tau_{w,x}$ [Pa], (Middle) $\tau_{w,z}$ [Pa], and (Lower) q_w [W/m^2] from the Mach 2 simulation with SA.

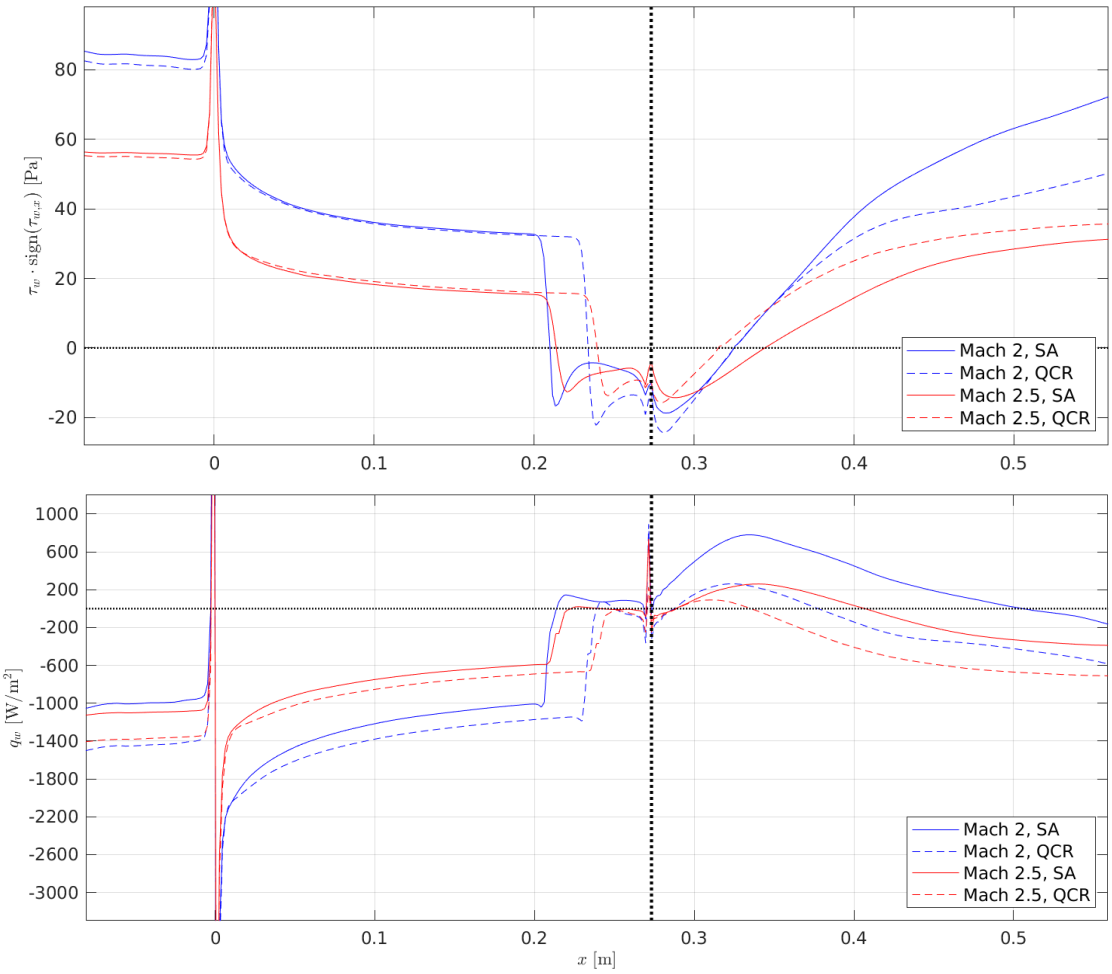

Fig. 8 Streamwise traces of (Upper) $\tau_w \mathrm{sign}(\tau_{w,x})$ and (Lower) q_w along the tunnel centerline. The dotted line at $x = 0.272$ m indicates the location of the compression corner.

IV. Conclusions and Recommendations

Two RANS models were used to conduct a simple sensitivity study of what we may expect to see in the forthcoming wind tunnel experiments. Given that these simulations were done completely blind to any actual wind tunnel data, it was fully expected that discrepancies would be found between the models and then between the simulated data and collected data. Once data have been collected comparisons will be made between those and the simulations reported herein. These simulations also provide an opportunity to organize the test procedures towards collecting useful data at pertinent locations within the flow. To this end, the following list includes recommendations for what would constitute the ideal set of experimental data to which direct comparisons would be made and which would best facilitate the development and validation of new turbulence closure models:

1) Particle Image Velocimetry (PIV) (2D, but preferably stereoscopic) should be collected on the tunnel centerplane from 5δ upstream of the ramp to downstream of the farthest expected reattachment location ($x = 0.375$). This will be used for flow topology identification (e.g., shock slope comparisons), upstream boundary layer matching, velocity magnitude comparisons, and separation, recirculation, and reattachment behavior.
2) PIV on spanwise (y-z) planes across the tunnel at locations including $x = -5\delta$, $x = 0.2$ m, right in the compression corner, and at multiple locations between $x = 0.3$ and $x = 0.375$ m, depending on the observed mean reattachment location.
3) PIV on floor-aligned (x-z) planes at multiple y heights from above the separation location on the ramp ($y \approx -0.08$ m) to as close as can be obtained to the tunnel floor ($y = -0.153$).

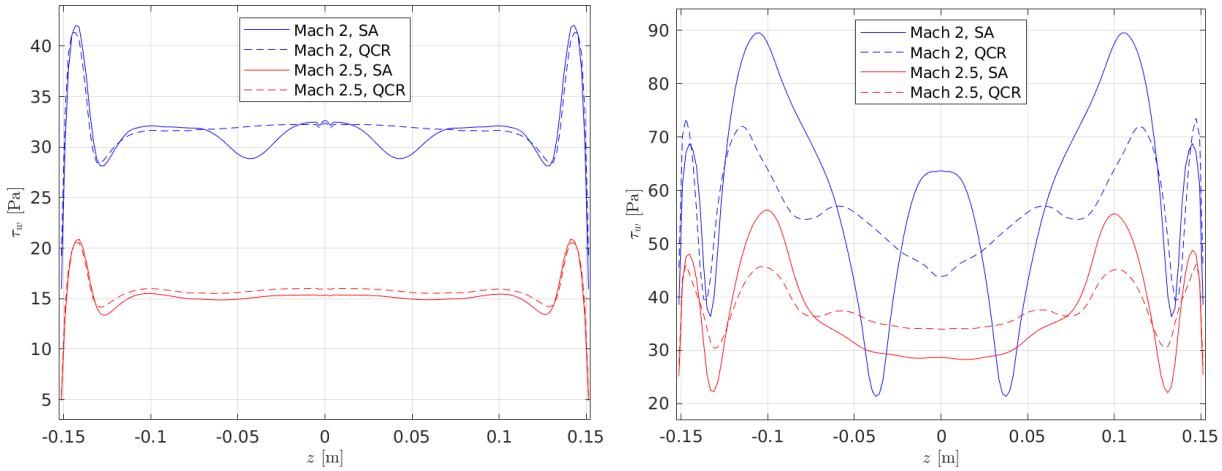

Fig. 9 Spanwise profiles of τ_w (Left) upstream of the separation at $x = 0.2$ m and (Right) downstream of reattachment at $x = 0.5$ m.

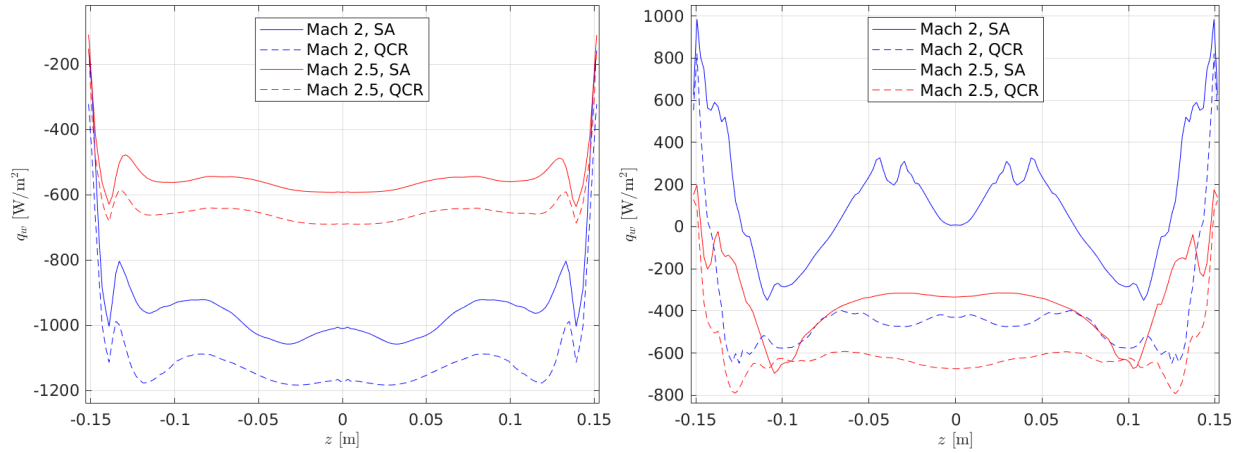

Fig. 10 Spanwise profiles of q_w (Left) upstream of the separation at $x = 0.2$ m and (Right) downstream of reattachment at $x = 0.5$ m.

4) Surface oil visualization should be used to identify the spanwise shape of the separation and reattachment lines on the ramp and on the tunnel floor, respectively. These will be used to compare both to the locations of the simulated lines as well as to the spanwise variations exhibited as functions of Mach number and closure model. Surface oil will also allow for wall streamline tracing in the complex 3D corner-corner flow region.
5) Oil Film Interferometry (OFI) on the ramp face and the tunnel floor. OFI cannot be used at the point of separation or reattachment but could be used in multiple zones upstream of separation, between the separation and reattachment lines, and downstream of reattachment [23].
6) Wall shear stress sensors in spanwise lines from sidewall to sidewall at multiple location on the ramp face and tunnel floor, from $x \approx 0.2$ m to $x \approx 0.45$ m.
7) Temperature sensitive paint (TSP) on the ramp face and on the downstream floor to identify the streamwise-oriented streak footprints that are indicative of the 3D roller structures expected in the flow.
8) Surface heat flux sensors in spanwise lines from sidewall to sidewall at multiple locations from the compression corner to $x \approx 0.45$ m. Ideally these will be roughly colocated with the shear stress sensors.
9) Surface pressure sensors in spanwise lines at multiple locations from upstream of the expected separation line, through the separated region, to the expected reattachment line. Both mean surface pressure and high-frequency unsteady pressure measurements will be useful for characterizing separation, the shock/boundary-layer interaction,

separation bubble breathing, reattachment, and general turbulence-induced pressure loading.

It is very likely that not all of these recommendations can be met during the experiments, due to a variety of complications like optical access, sensor sizes, tunnel and plenum geometry, and scheduling windows. For example, placing shear stress sensors into the ramp near the separation line is likely not possible and the optical access that would be needed for OFI in the same region may also be geometrically impossible. It is also very likely that not all of these measurements are needed to properly characterize the flow and/or to inform turbulence modeling efforts. Decision making on this front is ongoing as the experiments get underway.

Regardless, future work will include further investigation of the simulation data and in-depth comparisons to as much experimental data as are able to be collected. Additionally, further RANS simulations may be performed if significant differences are noticed in inflow or boundary conditions, and/or if it is found that neither of the models used herein sufficiently represented the experimental flow and the testing of other models or further calibrations of these models is justified. Additionally, scale-resolving simulations (likely wall-modeled and wall-resolved Large-Eddy Simulations) are planned for these cases as a way to provide more granular near-wall turbulence data that will also be used in the development of improved turbulence models. These will also allow for statistical comparisons of unsteadiness around the observed mean flow. This may include phenomena like shock motion, shear layer oscillations, and separation bubble breathing.

Finally, we make a note on flow relaminarization around the expansion corner. While multiple parameters have been used as indicators of flow relaminarization, the pressure gradient parameter ($K = \nu U_e^{-2} dU_e/dx$) of Launder [34] is perhaps the most used (e.g., [35]). A critical value of 3e-6 is typically defined as the threshold for the onset of relaminarization but it has been shown that relaminarization can begin prior to the critical value being reached [23]. It is also not clear how applicable K is to a sudden expansion in a supersonic flow and it should also always be presented in context with turbulence intensity. Additionally, values of K calculated from RANS data may not truly indicate relaminarization due to the approximate nature of the closure equations. Regardless of these caveats, values for K were calculated from the simulations and a maximum value of 8e-7 was found just downstream of the expansion corner (x = 3 cm) in the Mach 2.0, SA simulation. This likely indicates that some turbulence damping is occurring, but it is difficult to say whether full relaminarization is or is not likely based solely on this. Assessment of the potential for relaminarization is still clearly ongoing, and future work will include analyzing profiles taken from the PIV data to assess the turbulence intensity and the level to which relaminarization is occurring prior to the shock/boundary-layer interaction just upstream of the compression corner.

Acknowledgements

This work was supported by the United States Department of Energy via multiple sub-programs under SNL's Advanced Simulation and Computing (ASC) program. Sandia National Laboratories is a multi-mission laboratory managed and operated by National Technology & Engineering Solutions of Sandia, LLC (NTESS), a wholly owned subsidiary of Honeywell International Inc., for the U.S. Department of Energy's National Nuclear Security Administration (DOE/NNSA) under contract DE-NA0003525. This written work is authored by an employee of NTESS. The employee, not NTESS, owns the right, title and interest in and to the written work and is responsible for its contents. Any subjective views or opinions that might be expressed in the written work do not necessarily represent the views of the U.S. Government. The publisher acknowledges that the U.S. Government retains a non-exclusive, paid-up, irrevocable, world-wide license to publish or reproduce the published form of this written work or allow others to do so, for U.S. Government purposes. The DOE will provide public access to results of federally sponsored research in accordance with the DOE Public Access Plan.

References

[1] Narasimha, R., and Viswanath, P. R., "Reverse Transition at an Expansion Corner in Supersonic Flow," *AIAA Journal*, Vol. 13, No. 5, 1975, pp. 693–695. https://doi.org/10.2514/3.49793.

[2] Dussauge, J. P., and Gaviglio, J., "The rapid expansion of a supersonic turbulent flow: role of bulk dilatation," *J. Fluid Mech.*, Vol. 174, 1987, pp. 81–112. https://doi.org/10.1017/S0022112087000053.

[3] Zheltovodov, A. A., Shilein, É. K., and Horstman, C. C., "Development of separation in the region where a shock interacts with a turbulent boundary layer perturbed by rarefaction waves," *J. Appl. Mech. Tech. Phys.*, Vol. 34, No. 3, 1993, pp. 346–354. https://doi.org/10.1007/BF00864786.

[4] Fang, J., Yao, Y., Zheltovodov, A. A., Li, Z., and Lu, L., "Direct numerical simulation of supersonic turbulent flows around a tandem expansion-compression corner," *Phys. of Fluids*, Vol. 27, 2015, p. 125104. https://doi.org/10.1063/1.4936576.

[5] Xie, Z., Xiao, Z., Wang, G., and Yang, Y., "Direct numerical simulation of the effects of Reynolds number in Mach 2.9 flows over an expansion–compression corner," *Phys. of Fluids*, Vol. 34, 2022, p. 125129. https://doi.org/10.1063/5.0131991.

[6] Kianvashrad, N., and Knight, D., "Large Eddy Simulation of Shock Wave Boundary Layer Interaction in an Expansion-Compression Corner," *AIAA Paper 2023-1428*, 2023. https://doi.org/10.2514/6.2023-1428.

[7] Vogel, E. A., Coder, J. G., Chynoweth, B. C., and Schneider, S. P., "Experimental and Computational Results of a Cone-Slice-Ramp Geometry at Mach 6," *AIAA Paper 2019-3593*, 2019. https://doi.org/10.2514/6.2019-3593.

[8] Vogel, E. A., Ali, R. M., and Coder, J. G., "Time-Accurate LES of a Cone-Slice-Ramp at Mach 6," *AIAA Paper 2020-0032*, 2020. https://doi.org/10.2514/6.2020-0032.

[9] McKiernan, G. R., and Schneider, S. P., "Instability and Transition on a Cone with a Slice and Ramp at Mach 6," *AIAA paper 2021-0249*, 2021. https://doi.org/10.2514/6.2021-0249.

[10] Sadagopan, A., Huang, D., Jirasek, A., Seidel, J., Pandey, A., and Casper, K. M., "Joint Experimental/Computational Study of Fluid-Thermal-Structural Interaction of a Cone-Slice-Ramp in Hypersonic Flow," *AIAA Paper 2022-0291*, 2022. https://doi.org/10.2514/6.2022-0291.

[11] Pandey, A., Casper, K. M., Spillers, R., Soehnel, M., and Spitzer, S., "Hypersonic Shock Wave-Boundary-Layer Interaction on the Control Surface of a Slender Cone," *AIAA Paper 2020-0815*, 2020. https://doi.org/10.2514/6.2020-0815.

[12] Pandey, A., Jirasek, A., Seidel, J., Saltzman, A. J., Casper, K. M., Beresh, S. J., Bhakta, R., Denk, B. P., De Zetter, M. E., Spillers, R., Molinaro, N. J., and Meritt, R. J., "Relaminarization Effects on a Three-Dimensional Cone-Slice-Ramp Geometry at Mach 8," *AIAA Paper 2023-0269*, 2023. https://doi.org/10.2514/6.2023-0269.

[13] Tichenor, N. R., Humble, R. A., and Bowersox, R. D. W., "Response of a hypersonic turbulent boundary layer to favourable pressure gradients," *J. Fluid Mech.*, Vol. 722, 2013, pp. 187–213. https://doi.org/10.1017/jfm.2013.89.

[14] Nicholson, G. L., Huang, J., Duan, L., Choudhari, M. M., and Bowersox, R. D. W., "Simulation and Modeling of Hypersonic Turbulent Boundary Layers Subject to Favorable Pressure Gradients due to Streamline Curvature," *AIAA Paper 2021-1672*, 2021. https://doi.org/10.2514/6.2021-1672.

[15] Knight, D., Yan, H., Panaras, A., and Zheltovodov, A., "Advances in CFD prediction of shock wave turbulent boundary layer interactions," *Progress in Aerospace Sciences*, Vol. 39, No. 2, 2003, pp. 121–184. https://doi.org/10.1016/S0376-0421(02)00069-6.

[16] Childs, R. E., Stremel, P. M., Hawke, V. M., Garcia, J. A., Alter, S. J., C., H., Kleb, W. L., Parikh, P., Patel, M., Rhode, M. N., and Salari, K., "Flow characterization of the NASA Langley Unitary Plan Wind Tunnel, Test Section 2: Computational Results," *AIAA Paper 2021-2963*, 2021. https://doi.org/10.2514/6.2021-2963.

[17] Casper, M., K, Wagner, J. L., Beresh, S. J., Henfling, J. F., Spillers, R. W., and Pruett, B. O. M., "Complex Geometry Effects on Cavity Resonance," *AIAA Journal*, Vol. 54, No. 1, 2016, pp. 320–330. https://doi.org/10.2514/1.J054273.

[18] Beresh, S. J., Henfling, J. F., and Spillers, R. W., "Time-Resolved Planar Velocimetry of the Supersonic Wake of a Wall-Mounted Hemisphere," *AIAA Journal*, Vol. 57, No. 4, 2019, pp. 1383–1399. https://doi.org/10.2514/1.J057814.

[19] Ray, J., Kieweg, S., Dinzl, D., Carnes, B., Weirs, V. G., Freno, B., Howard, M., Smith, T., Nompelis, I., and Candler, G. V., "Estimation of Inflow Uncertainties in Laminar Hypersonic Double-Cone Experiments," *AIAA Journal*, Vol. 58, No. 10, 2020, pp. 4461–4474. https://doi.org/10.2514/1.J059033.

[20] Miller, N. E., Guildenbecher, D. R., and Lynch, K. P., "Aero-Optical Distortions of Turbulent Boundary Layers: DNS up to Mach 8," *AIAA Paper 2021-2832*, 2021. https://doi.org/10.2514/6.2021-2832.

[21] Lance, B. W., Krueger, A. M., Freno, B. A., and Wagnild, R. M., "Validation Study of the Multi-Fidelity Toolkit," *AIAA Paper 2022-1574*, 2022. https://doi.org/10.2514/6.2022-1574.

[22] Lynch, K. P., Miller, N. E., Barone, M. F., Beresh, S. J., Spillers, R. W., Henfling, J. F., and Soehnel, M. M., "Revisiting Bachalo-Johnson: The Sandia Axisymmetric Transonic Hump and CFD Challenge," *AIAA Paper 2019-2848*, 2019. https://doi.org/10.2514/6.2019-2848.

[23] Lynch, K. P., Lance, B. W., Miller, N. E., Barone, M. F., and Beresh, S. J., "Experimental Characterization of an Axisymmetric Transonic Separated Flow for Computational Fluid Dynamics Validation," *AIAA Journal*, Vol. 61, No. 4, 2023, pp. 1623–1637. https://doi.org/10.2514/1.J062278.

[24] Dandois, J., "Improvement of Corner Flow Prediction Using the Quadratic Constitutive Relation," *AIAA Journal*, Vol. 52, No. 12, 2014, pp. 2795–2806. https://doi.org/10.2514/1.J052976.

[25] Leger, T., Bisek, N., and Poggie, J., "Supersonic Corner Flow Predictions Using the QuadraticConstitutive Relation," *AIAA Journal*, Vol. 54, No. 7, 2016, pp. 2077–2088. https://doi.org/10.2514/1.J054732.

[26] Abe, H., Mizobuchi, Y., and Matsuo, Y., "Effect of a Quadratic Constitutive Relation on Juncture Flow Computations," *AIAA Paper 2020-2752*, 2020. https://doi.org/10.2514/6.2020-2752.

[27] Spalart, P. R., "Strategies for turbulence modelling and simulations," *Int. J. Heat Fluid Flow*, Vol. 21, No. 3, 2000, pp. 252–263. https://doi.org/10.1016/S0142-727X(00)00007-2.

[28] Rumsey, C. L., "Compressibility Considerations for $k-\omega$ Turbulence Models in Hypersonic Boundary-Layer Applications," *J. Spacecraft Rockets*, Vol. 47, No. 1, 2010. https://doi.org/10.2514/1.45350.

[29] White, F. M., *Viscous Fluid Flow*, McGraw Hill, New York, 2006.

[30] Sabnis, K., Babinsky, H., Galbraith, D. S., and Benek, J. A., "Nozzle Geometry-Induced Vortices in Supersonic Wind Tunnels," *AIAA Journal*, Vol. 59, No. 3, 2021, pp. 1087–1097. https://doi.org/10.2514/1.J059708.

[31] Bisek, N. J., "Sidewall Interaction of a Supersonic Flow over a Compression Ramp," *AIAA Paper 2015-1976*, 2015. https://doi.org/10.2514/6.2015-1976.

[32] Williams, R. D., and Babinsky, H., "Corner effects for compression corner shock wave/boundary layer interactions in rectangular channels," *AIAA Paper 2021-1312*, 2021. https://doi.org/10.2514/6.2021-1312.

[33] Zhuang, Y., Tan, Y.-Z., H-J. and. Liu, Zhang, Y.-C., and Ling, Y., "High resolution visualization of Görtler-like vortices in supersonic compression ramp flow," *J. Vis.*, Vol. 20, 2017, pp. 505–508. https://doi.org/10.1007/s12650-016-0415-1.

[34] Launder, B. E., "Laminarization of the turbulent boundary layer in a severe acceleration," *J. Appl. Meteor.*, Vol. 31, 1964, pp. 707–708. https://doi.org/10.1115/1.3629738.

[35] Mukund, R., Viswanath, P. R., Narasimha, R., Prabhu, A., and Crouch, J. D., "Relaminarization in highly favourable pressure gradients on a convex surface," *J. Fluid Mech.*, Vol. 566, 2006, pp. 97–115. https://doi.org/10.1017/S0022112006002473.